communications earth & environment

ARTICLE

https://doi.org/10.1038/s43247-023-00907-1 OPEN

Anthropogenic warming has exacerbated droughts in southern Europe since the 1850s

Wenling An[1,2], Chenxi Xu[1,2✉], Slobodan B. Marković[3,4], Shanlei Sun[5], Yue Sun[5], Milivoj B. Gavrilov[3], Zoran Govedar[6], Qingzhen Hao[1,2] & Zhengtang Guo[1,2]

Widespread and frequent droughts have affected most parts of Europe over recent years, but it remains unclear when this synchronous drying trend began and how it has been influenced by anthropogenic forcing. Here we reconstruct and explore the history of drought in southern Europe over the past 300 years using an annual record of tree-ring oxygen isotopes from a site in Bosnia and Herzegovina. The reconstruction suggests that the onset of the drying trend in southern Europe occurred around the 1850s, which is consistent with previous studies demonstrating the extensive and long-lasting drying across central and western European areas. The evidence from CMIP6 model and reanalysis data demonstrates that anthropogenic warming has enhanced the strength of land–atmosphere coupling and exacerbated the widespread drying trend since the 1850s.

[1] Key Laboratory of Cenozoic Geology and Environment, Institute of Geology and Geophysics, Chinese Academy of Sciences, Beijing, China. [2] CAS Center for Excellence in Life and Paleoenvironment, Beijing, China. [3] Faculty of Science, University of Novi Sad, Trg Dositeja Obradovića 3, 21000 Novi Sad, Serbia. [4] Serbian Academy of Sciences and Arts, Belgrade, Serbia. [5] Collaborative Innovation Center on Forecast and Evaluation of Meteorological Disasters/Key Laboratory of Meteorological Disaster, Ministry of Education/International Joint Research Laboratory on Climate and Environment Change, Nanjing University of Information Science & Technology (NUIST), Nanjing, China. [6] Faculty of Forestry, University of Banja Luka, Banja Luka, Republic of Srpska, Bosnia and Herzegovina. ✉email: cxxu@mail.iggcas.ac.cn

In 2022, an unusually severe drought began in May and expanded and worsened through the summer, affecting most parts of Europe[1]. Such extensive and synchronous summer droughts have occurred frequently over Europe since the 2000s and have caused major socioeconomic, agricultural, and ecosystem damage, and even loss of human life[2–5]. More than half of Europe may have been affected by extreme drought conditions over the past five years (2015–2019)[6]. Therefore, a better understanding of drought characteristics and their potential mechanisms at the European level is essential if we are to improve future drought prediction and mitigation.

Across Europe, the southern region is the area most vulnerable to droughts, especially at annual to decadal scales[7–11], whereas central Europe is the transition area between the wetting northern and drying southern regions[12,13]. Nevertheless, central Europe has also experienced evident drying in the recent century (Fig. 1), with increasing temperatures and decreasing precipitation (Supplementary Fig. 1) and many severe droughts[14–16]. Moreover, climate projections indicate that Europe will become one of the hotspots for future high-intensity droughts and prolonged heatwaves, with southern and central Europe becoming increasingly dry and hot[17,18]. However, owing to the short length of the observational record, it remains unclear when the widespread drying that is evident over most of Europe began, and how warming induced by greenhouse gas effect has influenced this trend when compared with natural variability.

Several proxy records spanning past centuries have recorded summer hydroclimatic variability over Europe[19–22]. The high-resolution tree ring-based Old World Drought Atlas (OWDA)[23] highlights some multidecadal periods of drought and wetness over large areas of Europe, but the mixing of winter hydroclimatic signals[24] makes it difficult to capture the full range of natural hydroclimatic variability during the summer season. Therefore, an extended network of summer or warm-season reconstructions covering the Europe is necessary. To address this knowledge gap, it is essential to use natural archives sensitive to the warm season dry-wet variations, to obtain more hydroclimate reconstruction that cover time periods before and after the start of industrialization.

Here we present a spring–summer dry/wet-sensitive tree ring oxygen isotope ($\delta^{18}O$) record from southern Europe covering the period 1711–2019 CE. Our record documents a persistent drying trend across southern Europe over the past 300 years, as well as recent drought intensification. Compared with previous drought reconstructions, we demonstrate that this widespread drying over most parts of Europe actually began in the 1850s, which coincides with the onset of anthropogenically generated greenhouse gas emissions. This drying trend agrees with the higher land-atmosphere coupling strength deduced from simulations under greenhouse gas (GHG) forcing, compared to that under natural (NAT) forcing. Moreover, enhanced land-atmosphere coupling, associated with a persistent soil moisture deficit, appears to have intensified surface warming, which has resulted in the recent drought exacerbation.

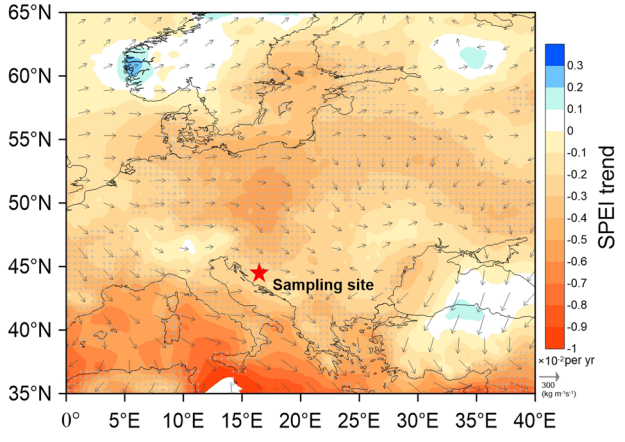

Fig. 1 Map showing the location of the sampling site (red star) and the European drought pattern. The color contours represent standardized precipitation–evaporation index (SPEI) trends for April–August (linear trend per year, from 1901 to 2019 CE). The gray crosses indicate trends significant at the 95% confidence level. The arrows indicate the average of the vertically integrated water vapor flux ($kgm^{-1}\,s^{-1}$) and its transport direction from April to August during 1948–2019 CE.

Results

The mean $\delta^{18}O$ values obtained from the five trees ranged from 28.8‰ to 29.4‰, which are similar to values obtained from trees in central Europe[20]. The individual raw $\delta^{18}O$ series displayed strong coherency with each other (Supplementary Table 1). The regional $\delta^{18}O$ chronology has an expressed population signal (EPS) of 0.89 and a mean correlation between series (Rbar) of 0.66 (Supplementary Fig. 2), indicating that the trees within the chronology possessed a common signal[25]. To establish a composite chronology, the five individual $\delta^{18}O$ series were normalized over their common period rather than simply averaging. This avoids some artificially abrupt increases or decreases in $\delta^{18}O$ values resulting from differences in the average $\delta^{18}O$ values between different trees (Supplementary Fig. 2). The period 1711–1739 CE was also presented in the composite chronology to evaluate the long-term trend, despite there being only one core for this period.

Hydroclimatic sensitivity of tree ring $\delta^{18}O$. The $\delta^{18}O$ values show a broad spatial representativeness of the April–August hydroclimatic conditions over most parts of southern Europe (south of 45°N), including Bosnia and Herzegovina, and neighboring regions in Serbia, Albania, Romania, Bulgaria, Greece and Italy (Fig. 2a). Therefore, we tested the climatic response of tree ring $\delta^{18}O$ variations to the averaged regional climate (10°E–25°E, 35°N–45°N). The regional $\delta^{18}O$ values correlate well with the monthly temperature variations (Pearson's r ranges from 0.31 to 0.51) from April to August, as well as with the monthly precipitation variations (Pearson's r ranges from −0.26 to −0.40) from June to August (Supplementary Fig. 3). There is a statistically significant correlation between the $\delta^{18}O$ chronology and the monthly standardized precipitation–evapotranspiration index[25] (SPEI, Methods, Supplementary Fig. 3). The strongest correlation was found between the $\delta^{18}O$ chronology and the mean April–August SPEI ($r = -0.70$, $p < 0.001$) during the period of 1901-2019, which increases to −0.72 and −0.71 when independently calculated over two contiguous instrumental periods; i.e., the early (1901–1959) and late (1960–2019) periods, respectively. This significant sensitivity of tree ring $\delta^{18}O$ is higher than that of southern European tree ring $\delta^{18}O$ from the ISONET project ($r = 0.2$-0.6, 1901-1998)[26]. When using the first differences of the time series, the correlation coefficients between the regional $\delta^{18}O$ and mean April–August temperature ($r = 0.45$, $p < 0.001$) and precipitation ($r = -0.57$, $p < 0.001$), as well as SPEI ($r = -0.59$, $p < 0.001$), remained high. These results indicate that the $\delta^{18}O$ chronology is sensitive to regional high- and low-frequency hydroclimatic variations.

Tree ring $\delta^{18}O$ values are influenced mainly by the stable isotope composition of precipitation (source water) and the evaporative enrichment of leaf water $\delta^{18}O$[27]. The precipitation $\delta^{18}O$ is controlled primarily by local precipitation–evapotranspiration processes[28]; consequently, tree ring $\delta^{18}O$ records the local drought history.

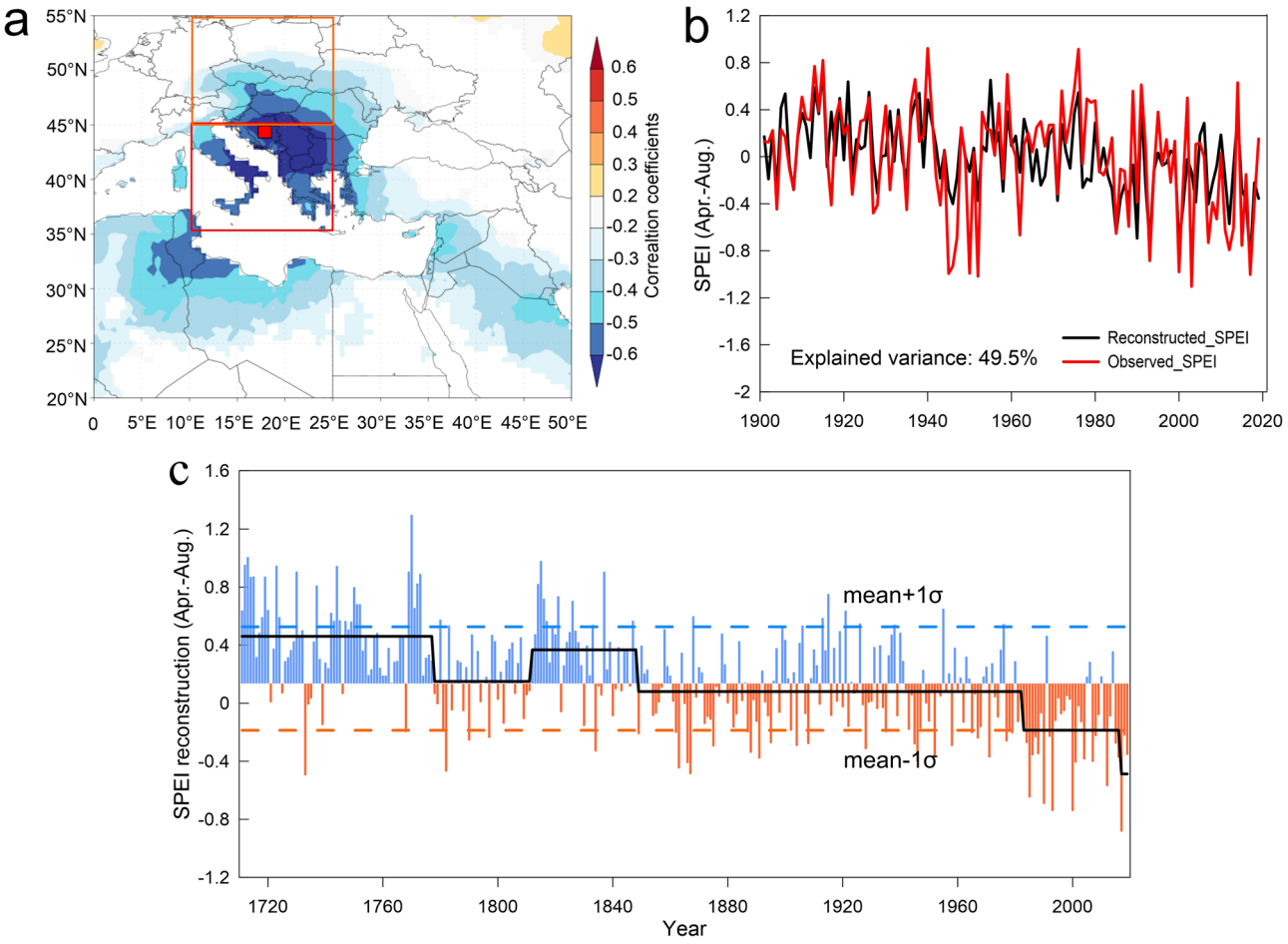

Fig. 2 Reconstructed southern European SPEI. Spatial correlations between tree ring $\delta^{18}O$ and observed April–August SPEI over Europe (**a**), and the red and orange rectangle indicates the boundaries of the southern and central European regions defined in this study, respectively (see Methods). Temporal variations between reconstructed and observed April–August SPEI (**b**) over the period 1901–2019. The reconstructed southern European SPEI variability (April–August) based on tree ring $\delta^{18}O$ over the past 309 years (**c**), the black solid line is the regime shifts (window length = 10 year, confident at 95%), and the blue and orange horizontal dashed lines represent the mean ±1σ (standard deviation) for this period.

Further isotopic fractionation that occurs in leaves is driven mainly by the difference between internal and external water vapor pressures[29], and thus by relative humidity. Dry conditions during growing season thus result in higher $\delta^{18}O$ values in leaf sugars, and consequently in wood cellulose. Therefore, a negative correlation between tree ring $\delta^{18}O$ and the SPEI index is expected. This is consistent with previous findings from other European regions[20, 30,31].

It is worth mentioning that our $\delta^{18}O$ values record the spring and summer drought signal, whereas some previous tree ring $\delta^{18}O$ values reflected mainly summer drought variations. This difference may be because, in this study, we used the whole wood cellulose from black pine (*Pinus nigra*) trees, which would contain the climate signal recorded during the early growing season, whereas other studies used latewood cellulose from oak trees (*Quercus robur*)[20,30]. A negative relationship between our pine $\delta^{18}O$ and spring–summer precipitation has been found in the adjacent regions of Montenegro, Bosnia, and Herzegovina[32].

Southern European warm season SPEI reconstruction from tree ring $\delta^{18}O$. Based on the strong correlation between tree ring $\delta^{18}O$ and the April–August SPEI, we used the $\delta^{18}O$ chronology to reconstruct the regional April–August SPEI over the past 300 years. Using a split period calibration and verification technique (see Methods), our reconstruction captures the full range of the instrumental April–August SPEI between 1901 and 2019 (Supplementary Table 2). All of the calibration and verification statistics confirm the temporal stability of the highly significant agreement between the reconstructed and measured April–August SPEI (Fig. 2b). The reconstructed SPEI variations identified two wet (1711–1778 and 1813–1849 CE) and two dry (1779–1812 and 1850–2019 CE) intervals. In general, the reconstruction is characterized by a gradually drying trend since the 1850s, and this drying tend persists to the present (Fig. 2c). Moreover, the recent drought intensification observed in the instrumental data[9] was evident in our reconstruction, and the long-term reconstruction further indicated that recent decades have experienced the most severe drought in southern Europe over the past 300 years, and with no wet years since 1976 (Supplementary Fig. 4).

Our reconstruction showed a significant but weak correlation with the July-August SPEI reconstruction for the southern Europe[26] ($r = 0.27$, $p < 0.001$, 1711–2018) using ISONET project isotope data (gridded ISONET reconstruction)[33–35]. The ISONET reconstruction only captured the drying trend in recent decades (Fig. S5). The correlation between our reconstruction and ISONET reconstruction was relatively low during the period of before 1900s ($r = 0.16$, $p > 0.05$). This indicated that the coherence between the two SPEI reconstructions was not strong before recent century. The different signal window (i.e., April–August vs July-August) and site-specific reconstruction may cause this discrepancy.

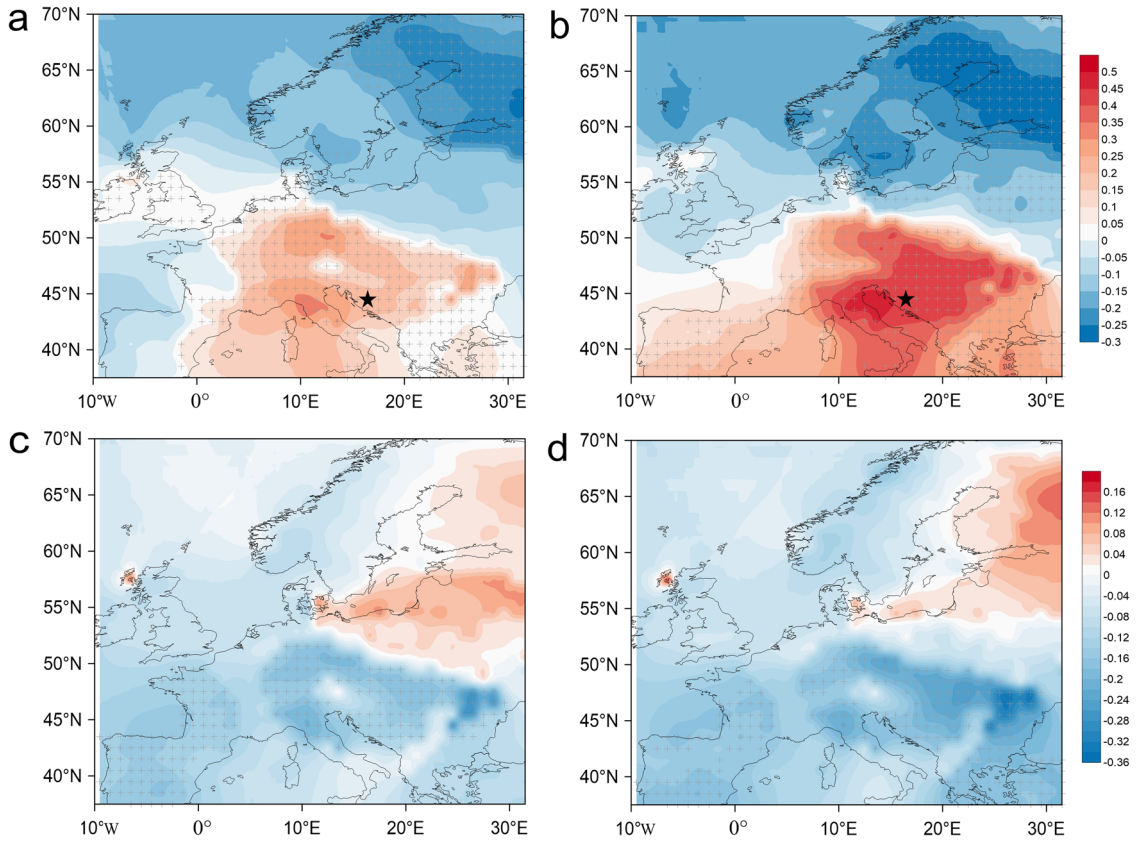

Fig. 3 Dipole-like dry-wet pattern over Europe. Spatial correlation for the SPEI reconstruction between southern Europe (this study) and the gridded ISONET reconstruction[26] during the period 1711–2018 (**a**) and 1850–2018 **b**. Spatial correlation between the gridded ISONET reconstruction[26] and winter NAO index[63] during the period 1711–2018 (**c**) and 1850–2018 (**d**). The black star in **a**, **b** indicates the sampling site in this study. The gray dots represent trends significant at the 95% confidence level.

Dipole-like drought structure over Europe. We compared our reconstruction with previously published summer dry-wet reconstructions over Europe[19,20,31,36]. Overall, most European region showed a drying trend since about the 1850s (Supplementary Fig. 6)[31], despite some detailed offsets in trends caused by the seasonal differences between these reconstructions. However, the southern and northern Europe dry-wet variation shows almost opposite multidecadal trend since the 1850s (Supplementary Fig. 6), with a wetting trend recorded in the north European reconstruction since the 1900s (Supplementary Fig. 6e). We further made spatial correlation between our reconstruction and gridded ISONET reconstruction (July-August SPEI) for the Europe. The spatial correlation shows that our reconstruction is significantly and positively correlation with southern European SPEI (Fig. 3a, b), while negative correlations with northern European SPEI over the past 300 years (Fig. 3a, b).

This dipole-like drought structure could be caused by the changes in the North Atlantic Oscillation (NAO), which is the main atmospheric circulation pattern modulating the European climate[37–40] and has changed to patterns with more positive phases since around the 1850s (Supplementary Fig. 6f). During the positive phase of the NAO, the central and southern parts of Europe are dominated by a high-pressure center associated with stronger anticyclonic circulation, while cyclonic conditions are prevailed in the northern Europe. This favors the advection of dry and warm air from the northern part of Africa toward the southeastern part of Europe, which results in extreme dry and hot summers[38]. The dipole-like pattern was also found between the spatial correlation fields of NAO and ISONET SPEI reconstruction. The NAO index showed negative correlation with the southern European SPEI during the past 300 years (Fig. 3c). In contrast, the stronger cyclonic circulation in the north would lead to positive precipitation anomalies and thus lead to wet northern Europe[38], and thus positive correlation between NAO and northern European SPEI was observed (Fig. 3c, d).

Extensive European drought and enhanced land-atmosphere coupling under anthropogenic warming. Despite the wetting of northern Europe, other regions over Europe have moved toward a drying environment since the 1850s (Supplementary Fig. 6), especially the southern and central Europe (Fig. 3a, b). Compared with other regions, both southern and central Europe show significant drought intensification in recent decades (Supplementary Fig. 6b, c). It indicates that the southern and central European droughts could have shared similar driving factors.

Extensive drought and aridity events can be caused by both large-scale atmospheric dynamics and local land-atmosphere feedbacks[41]. In Europe, the position of the North Atlantic Jet (NAJ) and duration of high-pressure cells over northern and central Europe may affect the spatiotemporal scale of the widespread European summer droughts[42, 43]. We found significant and stable relationships between southern European drought reconstruction and reconstructed NAJ variations (Supplementary Fig. 7). However, no relationship was detected between central European droughts and NAJ (Supplementary Fig. 7). It indicates that as the climate transition area, the influence of atmospheric circulation on central European drought could be complicated and unstable.

The local land-atmosphere feedbacks mainly contain soil moisture-temperature feedback and soil moisture-precipitation

feedback. It has been found that recent increasing drought severity in southern Europe is mainly related with temperature rise[9], and the enhanced coupling of soil moisture-temperature effects could have caused recent hotter-drier summers in some European region[19]. The significant increasing temperature trend was also detected in most Europe, while the precipitation decrease is only significant in the central Europe (Supplementary Fig. 1). Therefore, for the Europe, the soil moisture-temperature feedbacks could be the dominant mechanism of the land-atmosphere coupling, especially for the relatively arid area[44].

The rising surface temperature and related land-atmosphere coupling has been reported to increase evaporation and to reduce soil moisture, and thus promote greater drought. The reduced soil moisture would further favor increase of near-surface air temperature and therefore cause severe droughts[41,44,45]. Low soil moisture levels reduce evapotranspiration and increase the sensible heat flux. The reduction of evapotranspiration decreases moisture recycling and further increases the sensible heat flux, which may then increase atmospheric stability and inhibit cloud and precipitation formation[46]. This would result in a negative coupling between soil moisture and sensible heat: a reduction in soil moisture induces an increase in the sensible heat flux, which causes an increase in near-surface air temperature, and consequently leads to severe aridity.

Our results reveal the strong relationships between dry-wet variations of southern and central Europe and observational temperature (Supplementary Fig. 8), as well as soil moisture variations from GHG forcing models at annual to decadal scales. To investigate the influence of anthropogenic warming on the strength of the land-atmosphere coupling, we compared the strength of the regional land-atmosphere coupling ($I_{SM\text{-}T}$, Methods) from southern and central Europe using the Coupled Model Intercomparison Project Phase 6 (CMIP6) modeled atmospheric and land surface data (Supplementary Table 3). This metric quantifies the relationship between near-surface temperature anomalies and soil moisture deficits in the land surface energy balance. The regional range for southern and central Europe was determined from the spatial representativeness of the respective hydroclimatic reconstructions (see Methods). The CMIP6 multi-model (Supplementary Table 3) ensembles include experiments driven by natural-only forcing (NAT), GHG forcing, and historical forcing (ALL forcing). The results revealed that the land-atmosphere coupling strength in the GHG and ALL forcing experiments was significantly stronger than that generated by the NAT forcing. The difference in the coupling strength between the NAT and GHG forcing was between 58% and 59.1% for the southern and central Europe, respectively (Fig. 4a). Similarly, the correlation coefficients between the sensible heat flux and atmospheric temperature are much greater under the GHG and ALL forcing than under the NAT forcing (Fig. 4b). The soil moisture variations under the GHG forcing also show an evident decreasing trend in southern and central Europe, which is consistent with the drying trend seen in the reconstructions (Supplementary Fig. 8). Therefore, it can be inferred that anthropogenic GHG forcing has led to strengthened land-atmosphere coupling in central and southern Europe, which might be responsible for the persistent drying trend over both regions since the 1850s via land surface and atmospheric feedbacks.

The influence of land-atmosphere coupling on European drought intensification over recent decades was further quantified using another observationally based (π diagnostic) coupling between soil moisture and temperature[47] (see Methods). During the past six decades, the temporal variation of the coupling strength has followed a well-defined increasing trend over most of Europe, including the southern, central, and part of the northern regions (Fig. 5a). We note that the land-atmosphere coupling strength in southern Europe is generally greater than that in central Europe (Fig. 5b), where it is usually arid and evapotranspiration is mainly controlled by soil moisture, which implies stronger soil moisture-temperature feedback[45]. Moreover, both regions have shown an increasingly enhanced trend since the 2000s (Fig. 5b), which corresponds to recent drought intensification over the past two decades. In addition, compared with those years when only southern Europe suffered droughts (Fig. 5c), the coupling strengths are generally stronger when both regions experienced droughts simultaneously (Fig. 5d).

We did not perform a future projection, but it can be inferred that the human-induced widespread drying trend evident over most parts of Europe will persist under global warming. It is noted that with increasingly warming in recent century (Supplementary Fig. 1a, b), many parts of northern Europe also show a tendency towards dry conditions (Fig. 1). These findings imply that more frequent and severe droughts may occur simultaneously over most of European, which will present a significant challenge for the inhabitants of the affected regions. Further efforts are needed to provide a more detailed estimation of the SPEI magnitude and its influence on regional ecosystem in combination with other tree ring index and observations.

Methods

Sampling and local climate. Our sampling sites in the Dinaric Alps (44.15°–44.46°N, 16.47°–17.28°E) were located in the Lom rainforest (on Klekovača) and the Janj rainforest/reservation (on Stolovaš) at altitudes from 1115 m a.m.s.l. (above mean sea level) to 1250 m a.m.s.l., in the Republic of Bosnia and Herzegovina (Fig. 1). In October 2019, a single increment core was extracted at breast height from each of 24 European black pines (*Pinus nigra*). European black pine is widespread across southern Europe and can grow on steep, rocky slopes where the conditions are too extreme for other tree species. According to recent studies using the pinning method and manual band dendrometers, its growing season covers the whole of spring and summer, with wood formation starting in early to mid-March and xylem growth finishing from the middle of August to September[48]. *P. nigra* is not shade tolerant and can resist extreme climatic conditions such as summer heat and a lack of precipitation[49]. Climate data show that only 36% of the annual precipitation of 817 ± 94 mm falls during the growing season from April to August in the study area (Supplementary Fig. 9), and the moisture is derived mainly from the North Atlantic (Fig. 1). Therefore, tree ring cellulose $\delta^{18}O$ is expected to record a dry-wet signal during the growth season. Based on the regional representativeness of the SPEI reconstructions in this study, and also that from Büntgen, et al.[20] (Supplementary Fig. 10), we defined the southern and central European areas as falling within 10°–25°E, 35°–45°N and 10°–25°E, 46°–55°N, respectively, to facilitate the comparisons between the two regions.

Stable oxygen isotope chronology development. The sample cores were air-dried and polished using sand paper until the ring structure was clearly visible. The ring widths of all samples were measured using a LINTAB 6 measuring table (Rinntech, Heidelberg, Germany; with a precision of 0.01 mm), after which cross-dating was checked using the COFECHA software[50]. Based on accurate cross-dating, five cores from five different trees with wider rings and without evident growth disturbance were selected for isotope analysis. We used the modified plate method to extract α-cellulose[51] and followed the chemical treatment procedure of the Jayme–Wise method[52,53]. The whole wood alpha-cellulose of each tree ring was carefully split from the wood plate using a razor blade and a binocular microscope. The alpha-cellulose samples, weighing between 0.09 and 0.25 mg, were placed in silver foil. The $\delta^{18}O$ values were measured in a pyrolysis-type high-temperature conversion elemental analyzer (TC/EA, Thermo Scientific) linked to an isotope ratio mass spectrometer (Delta V Advantage, Thermo Scientific) at the Key Laboratory of Cenozoic Geology and Environment, Chinese Academy of Sciences, Beijing, China. The isotopic results for oxygen are presented in δ notation as per mil (‰) relative to the Vienna standard mean ocean water: $\delta^{18}O = (R_{sample}/R_{standard} - 1) \times 1000$, where R_{sample} and $R_{standard}$ are the $^{18}O/^{16}O$ ratios of the sample and standard, respectively. We measured 1582 cellulose samples, and the analytical uncertainties for repeated measurements of Merck cellulose were ~ ±0.15‰ ($n = 185$).

Climate reconstruction. The most reliable and representative period of the chronology was evaluated using the expressed population signal (EPS) and mean correlation between series (Rbar)[54]. In general, the EPS reflects how well a chronology represents a theoretically infinite population based on a finite sample

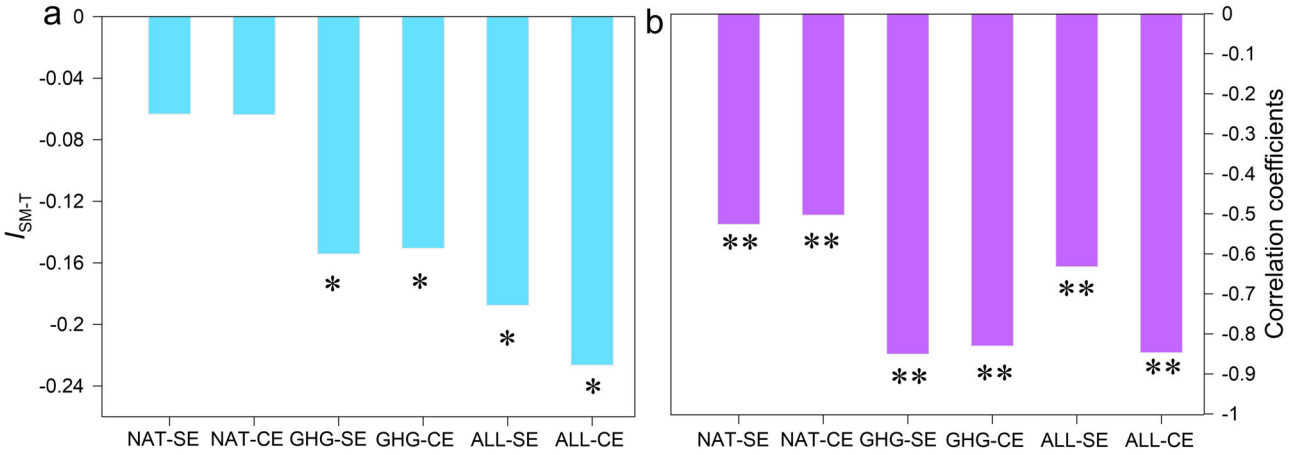

Fig. 4 Land-atmosphere coupling strength (I_{SM-T}) in CMIP6 model. The land-atmosphere coupling strength (**a**) calculated from ensemble means of 9 CMIP6 models between 1850–2019 CE, driven by natural-only forcing (NAT), greenhouse gas (GHG) forcing, and historical (ALL) forcing, and correlation coefficients between modeled sensible heat flux and atmospheric temperature (**b**). The I_{SM-T} is the land-atmosphere coupling strength based on the correlations between soil moisture and sensible heat flux, and the standard deviation of temperature (see Methods). The asterisk in **a** indicates that the land-atmosphere coupling strength differences between NAT forcing and GHG/ALL forcing are significant at 95% confidence level based on ANOVA analysis. The asterisk in **b** indicates the correlation coefficients exceed the 99% confidence level.

size, and Rbar provides an indication of the strength of the tree ring chronology signal. The commonly accepted threshold is EPS > 0.85[25]. The most reliable period is 1740–2019 CE, for which the threshold of 0.85 was reached at a sample depth in two cores (Supplementary Fig. 2). However, the period 1711–1739 was also presented in the reconstruction to evaluate the long-term trend, although there is only one core that covers this period. We calculated Pearson's correlation coefficient (r) between the tree ring $\delta^{18}O$ series and climate variables from the previous November to the current August. A linear model was developed to reconstruct the SPEI from April to August using the tree ring $\delta^{18}O$ values. The validity of the regression model was evaluated using statistics related to the calibration and verification periods. Evaluative verification was conducted using the correlation coefficient (r), coefficient of determination (R^2), reduction of error test (RE), coefficient of efficiency (CE), Sign test, and Durbin–Watson test (DW)[54]. R^2 and RE are both measures of shared variance between the climate and tree rings, and a positive RE is evidence of a valid regression model[55]. The DW statistic tests are for autocorrelation in the residuals between a model and the target hydrological data[56]. The sign test counts the number of agreements and disagreements between the reconstructed and instrumental climate data. In addition, one standard deviation from the mean was used as a threshold to detect extreme dry and wet events.

Climate and model data. We used monthly gridded (2.5° × 2.5°) pressure, wind, and specific humidity data from the NCEP/NCAR reanalysis data set[57] to analyze the direction and distribution of the total water vapor flux over Europe. We used monthly gridded temperature, precipitation Palmer Drought Index[58] (PDSI) from the Climatic Research Unit (CRU) gridded data set (TS4.05) with a grid size 0.5° × 0.5°[59,60] to assess climatic trends over Europe and then to explore the climatic sensitivity in the tree ring $\delta^{18}O$ series. Moreover, we obtained the monthly soil moisture (between depths of 0 and 10 cm) reanalysis data from the Global Land Data Assimilation System (GLDAS, https://ldas.gsfc.nasa.gov/gldas) to allow comparison with the reconstructed regional SPEI. The standardized precipitation–evaporation index (SPEI) is a multi-scalar drought index that estimates drought using water balance, calculated as precipitation minus evapotranspiration[60]. The calculation of SPEI takes temperature effects into account by introducing potential evapotranspiration. We found significant positive correlations between regional SPEI and PDSI ($r = 0.59$, $p < 0.001$) and soil moisture ($r = 0.67$, $p < 0.001$) (Supplementary Fig. 11). It has been suggested that in the Mediterranean, temperature effects via evapotranspiration need to be considered to produce meaningful indices representative of water deficit[61]. In the present study, we adopted the 0.5° gridded monthly SPEI data set for the study region. Moreover, the gridded ISONET reconstruction data set (July-August SPEI-02) for Europe was used to make comparisons[26]. This gridded data set is reconstructed from the ISONET project supported by the European Union (EVK2-CT-2002-00147'ISONET'). In addition, we made comparisons between the averaged April–August SPEI and August SPEI-05 values, and they showed very high consistencies ($r = 0.95$, $p < 0.001$) (Supplementary Fig. 12). This demonstrated that the results won't be influenced by using either the five-month SPEI values or the averages of the one-month SPEI values over April through August.

The soil moisture levels between depths of 0 and 10 cm, upward sensible heat flux, and near-surface temperature (2 m) from nine available CMIP6 experiments (https://esgf-data.dkrz.de/search/cmip6-dkrz/) over the period 1850–2020 were used to evaluate the regional land-atmosphere coupling strength since the 1850s. It has been reported that soil moisture from the CMIP6 is relatively accurate in trend evaluation, despite some differences among individual models[62]. In this study, we used a set of model simulations including the experiments driven by the natural-only forcing (NAT) and greenhouse gas (GHG) forcing, and historical forcing (ALL, natural + anthropogenic forcing) (Supplementary Table 3). The reconstructed winter (NAO)[63] was used to investigate the possible influence of the NAO on regional dry-wet variations.

The ERA5-Land Reanalysis data was also used to calculate the land-atmosphere coupling strength for Europe from 1959 to 2018. The ERA5-Land Reanalysis data is a global reanalysis data set of atmospheric, land, oceanic variables with high spatial- and temporal- resolutions, developed by the European Center for Medium-range Forecasting (ECMWF)[64]. ERA5-Land hourly data set (0.1° latitude × 0.1° longitude) over Europe are collected in this study and the near-surface air temperature, surface net radiation, actual latent heat flux, and potential evaporation are used in this study.

Statistical analysis. Pearson correlation analysis was used to explore the relationship between $\delta^{18}O$ and observed SPEI, temperature, and precipitation, as well as to compare our reconstruction with previous dry-wet reconstructions. We performed regime shift detection analysis[65] based on mean changes in the reconstruction. For this analysis, the cutoff regime length was set to 10, and we used the 95% confidence level. The dry (humid) years were defined as those years with a spring–summer SPEI of less (greater) than the mean of the whole period minus (plus) 1σ. To assess the spatial representativeness of the reconstruction, we calculated spatial correlations between the reconstruction and SPEI using the KNMI Climate Explorer (http://climexp.knmi.nl). ANOVA analysis was explored to test the significance of the differences in land-atmosphere coupling strength between NAT forcing and GHG/ALL forcing. The locally estimated scatterplot smoothing (LOESS) regression was used to derive the smoothed trend lines of the land-atmosphere coupling strength, and this method is suitable for data with outliers when a robust fitting method is necessary[66]. We also calculated the standardized values of land-atmosphere coupling strength (Z scores of π), to facilitate the comparisons.

Land-atmosphere coupling strength. In this study, we used two methods to evaluate the strength of the land-atmosphere coupling. The first metric was the two-legged index (I_{SM-T}), which uses the correlations between two variables (soil moisture and sensible heat flux) but adds the standard deviation of temperature (Eq. 1). This accounts for the possibility of a high correlation between two variables being coincident with low variability[67].

$$I_{SM-T} = \rho(SM, SH)\rho(SH, T)\sigma(T) \quad (1)$$

We used the monthly soil moisture (SM), sensible heat flux (SH), and near-surface air temperature (T), which we obtained from the CMIP6 models to calculate this two-legged index.

The second metric uses the π diagnostic of the land-atmosphere coupling strength to quantify the strength of the coupling between soil moisture and temperature. It is calculated as the product of the anomalies in the near-surface air temperature (T) and the anomalies in the effect of the soil moisture deficits in the

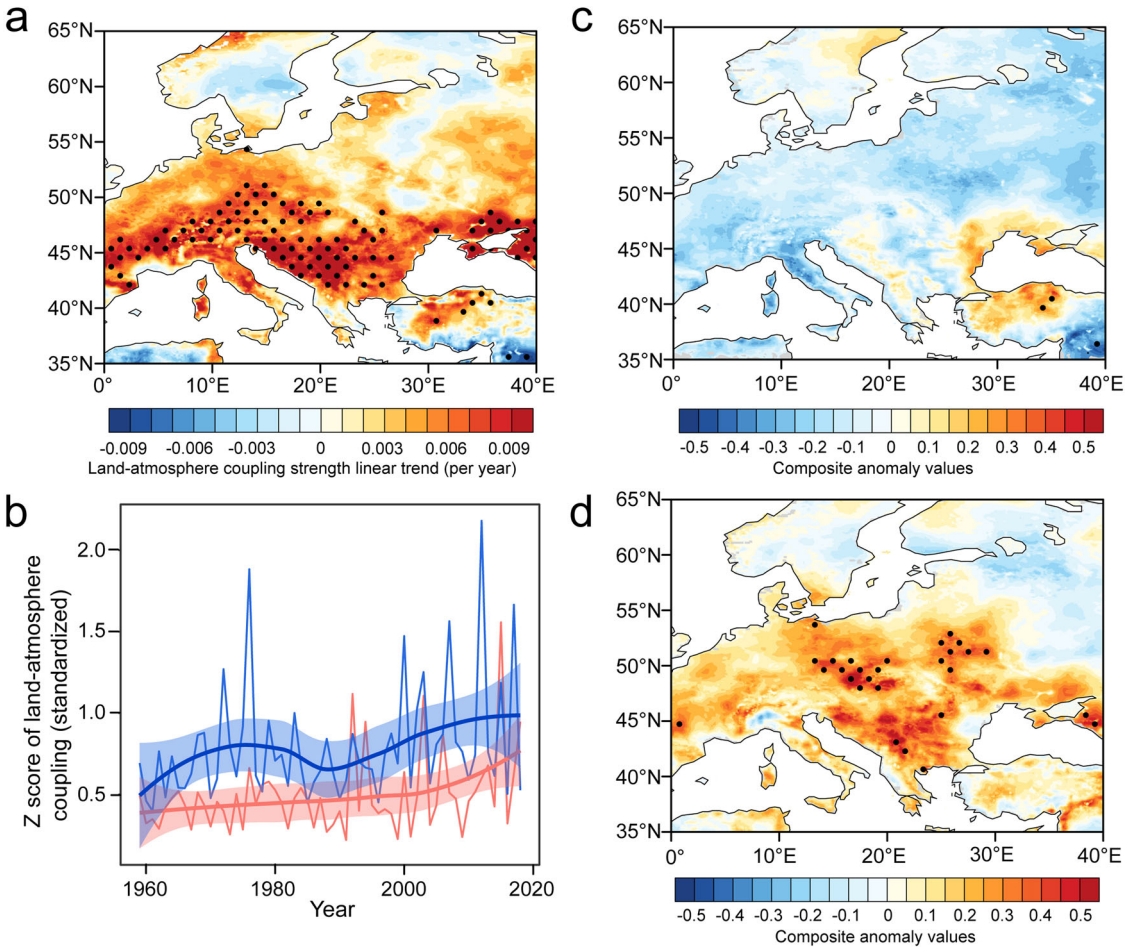

Fig. 5 Land-atmosphere coupling strength (π) from ERA5-land reanalysis data. Linear trends of June-August land-atmosphere coupling strength (π) over the period 1959–2018 CE (**a**). The inter-annual variation of June–August land-atmosphere coupling strength over the period 1959–2018 CE for central (light red lines) and southern Europe (light blue lines), trend lines are estimated using the non-parametric LOESS regression technique, and shading represents the 95% confidence intervals of the estimated trends (**b**). Composite anomaly map of summer coupling strength for the 8 identified dry years of southern Europe (**c**), and the 10 identified dry years of both southern and central Europe (**d**). The coupling strength is calculated based on the ERA5-Land reanalysis daily data set with 0.1° latitude × 0.1° longitude spatial resolution. Black dots in **a**, **c**, and **d** mark the grids where trends are significant at the 95% confidence level. The Z scores in **b** indicate the standardized values of land-atmosphere coupling strength (π), which is calculated to facilitate the comparisons.

land surface energy balance (e)[47], as follows:

$$\pi = e' \times T' = [(Rn - \lambda E)' - (Rn - \lambda Ep)']T' \quad (2)$$

where Rn represents the surface net radiation, λ refers to the latent heat of vaporization (which can be calculated as a function of T), λE is the actual latent heat flux, and λEp denotes the latent heat flux based on potential evaporation. T' and H' are daily anomalies of T and H, respectively. Data regarding T, Rn, E, and Ep were derived from the ERA5-Land hourly data set[64]. This method has been used to quantify summer soil moisture and temperature coupling strength in Europe[44,47] and other regions[68].

Data availability

The tree ring $\delta^{18}O$-based warm season SPEI reconstruction data in this study can be accessed from https://www.ncei.noaa.gov/access/paleo-search/study/38233, and https://doi.org/10.6084/m9.figshare.23544327. The CRU TS4.05 data set was from https://www.uea.ac.uk/groups-and-centres/climatic-research-unit. The NCEP/NCAR reanalysis monthly gridded data was from thttps://psl.noaa.gov/data/gridded/data.ncep.reanalysis. The GLDAS monthly soil moisture reanalysis data was from https://ldas.gsfc.nasa.gov/gldas. The gridded ISONET reconstruction data set was from https://doi.org/10.26188/21988628.v1. The ERA5-Land Reanalysis data was from https://cds.climate.copernicus.eu/cdsapp#!/dataset/reanalysis-era5-land. The CMIP6 model data was from https://esgf-data.dkrz.de/search/cmip6-dkrz/.

Received: 10 January 2023; Accepted: 22 June 2023;
Published online: 30 June 2023

References

1. Toreti, A. et al. Drought in Europe August 2022. (Publications Office of the European Union, 2022).
2. Senf, C., Buras, A., Zang, C. S., Rammig, A. & Seidl, R. Excess forest mortality is consistently linked to drought across Europe. *Nat. Commun.* **11**, 6200 (2020).
3. Gomez-Gener, L., Lupon, A., Laudon, H. & Sponseller, R. A. Drought alters the biogeochemistry of boreal stream networks. *Nat. Commun.* **11**, 1795 (2020).
4. Naumann, G., Cammalleri, C., Mentaschi, L. & Feyen, L. Increased economic drought impacts in Europe with anthropogenic warming. *Nat. Clim. Change* **11**, 485–491 (2021).
5. Amengual, A. et al. Projections of heat waves with high impact on human health in Europe. *Glob. Planet. Change* **119**, 71–84 (2014).
6. Ionita, M., Nagavciuc, V., Scholz, P. & Dima, M. Long-term drought intensification over Europe driven by the weakening trend of the Atlantic Meridional overturning circulation. *J. Hydrol. Reg. Stud.* **42** https://doi.org/10.1016/j.ejrh.2022.101176 (2022).
7. Caloiero, T., Veltri, S., Caloiero, P. & Frustaci, F. Drought analysis in Europe and in the Mediterranean basin using the standardized precipitation index. *Water* **10**, 1043 (2018).
8. Moravec, V., Markonis, Y., Rakovec, O., Kumar, R. & Hanel, M. A 250-year European drought inventory derived from ensemble hydrologic modeling. *Geophys. Res. Lett.* **46**, 5909–5917 (2019).
9. Vicente-Serrano, S. M. et al. Evidence of increasing drought severity caused by temperature rise in southern Europe. *Environ. Res. Lett.* **9** https://doi.org/10.1088/1748-9326/9/4/044001 (2014).

10. Jaagus, J. et al. Long-term changes in drought indices in eastern and central Europe. *Int. J. Climatol.* **42**, 225–249 (2021).
11. Gavrilov, M. B. et al. Aridity in the Central and Southern Pannonian Basin. *Atmosphere* **11** https://doi.org/10.3390/atmos11121269 (2020).
12. Spinoni, J., Vogt, J. V., Naumann, G., Barbosa, P. & Dosio, A. Will drought events become more frequent and severe in Europe? *Int. J. Climatol.* **38**, 1718–1736 (2018).
13. Stagge, J. H., Kingston, D. G., Tallaksen, L. M. & Hannah, D. M. Observed drought indices show increasing divergence across Europe. *Sci. Rep.* **7**, 14045 (2017).
14. Trnka, M. et al. Drought trends over part of Central Europe between 1961 and 2014. *Clim. Res.* **70**, 143–160 (2016).
15. Spinoni, J., Naumann, G., Vogt, J. V. & Barbosa, P. The biggest drought events in Europe from 1950 to 2012. *J. Hydrol. Reg. Stud.* **3**, 509–524 (2015).
16. Stojanovic, M., Drumond, A., Nieto, R. & Gimeno, L. Variations in moisture supply from the Mediterranean Sea during meteorological drought episodes over Central Europe. *Atmosphere* **9**, 278 (2018).
17. Balting, D. F., AghaKouchak, A., Lohmann, G. & Ionita, M. Northern Hemisphere drought risk in a warming climate. *npj Clim. Atmos. Sci.* **4** https://doi.org/10.1038/s41612-021-00218-2 (2021).
18. Lehner, F. et al. Projected drought risk in 1.5 °C and 2 °C warmer climates. *Geophys. Res. Lett.* **44**, 7419–7428 (2017).
19. Wang, L. et al. The 1820s marks a shift to hotter-drier summers in Western Europe Since 1360. *Geophys. Res. Lett.* **49** https://doi.org/10.1029/2022gl099692 (2022).
20. Büntgen, U. et al. Recent European drought extremes beyond Common Era background variability. *Nat. Geosci.* https://doi.org/10.1038/s41561-021-00698-0 (2021).
21. Chen, D. et al. Hydroclimate changes over Sweden in the twentieth and twenty-first centuries: a millennium perspective. *Geogr. Ann. A: Phys. Geogr.* **103**, 103–131 (2020).
22. Klippel, L. et al. A 1286-year hydro-climate reconstruction for the Balkan Peninsula. *Boreas* **47**, 1218–1229 (2018).
23. Cook, E. R. et al. Old World megadroughts and pluvials during the Common Era. *Sci. Adv.* **1**, e1500561 (2015).
24. Markonis, Y., Hanel, M., Maca, P., Kysely, J. & Cook, E. R. Persistent multi-scale fluctuations shift European hydroclimate to its millennial boundaries. *Nat. Commun.* **9**, 1767 (2018).
25. Wigley, T. M., Briffa, K. R. & Jones, P. D. On the average value of correlated time series, with applications in dendroclimatology and hydrometeorology. *J. Appl. Meteorol. Climatol.* **23**, 201–213 (1984).
26. Freund, M. B. et al. European tree-ring isotopes indicate unusual recent hydroclimate. *Commun. Earth Environ.* **4**, 26 (2023).
27. Roden, J. S., Lin, G. H. & Ehleringer, J. R. A mechanistic model for interpretation of hydrogen and oxygen isotope ratios in tree-ring cellulose. *Geochim. Cosmochim. Acta* **64**, 21–35 (2000).
28. Rozanski, K., Sonntag, C. & Münnich, K. O. Factors controlling stable isotope composition of European precipitation. *Tellus A: Dyn. Meteorol. Oceanogr.* **34** https://doi.org/10.3402/tellusa.v34i2.10796 (1982).
29. Gessler, A. et al. Stable isotopes in tree rings: towards a mechanistic understanding of isotope fractionation and mixing processes from the leaves to the wood. *Tree Physiol.* **34**, 796–818 (2014).
30. Nagavciuc, V. et al. Stable oxygen isotopes in Romanian oak tree rings record summer droughts and associated large-scale circulation patterns over Europe. *Clim. Dyn.* **52**, 6557–6568 (2018).
31. Nagavciuc, V., Ionita, M., Kern, Z., McCarroll, D. & Popa, I. A ~700 years perspective on the 21st century drying in the eastern part of Europe based on δ18O in tree ring cellulose. *Commun. Earth. Environ.* **3** https://doi.org/10.1038/s43247-022-00605-4 (2022).
32. Lukač, L. et al. Stable isotopes in tree rings of Pinus heldreichii can indicate climate variability over the Eastern Mediterranean Region. *Forests* **12**, 350 (2021).
33. Balting, D. F. et al. Large-scale climate signals of a European oxygen isotope network from tree rings. *Clim. Past* **17**, 1005–1023 (2021).
34. Treydte, K. et al. Signal strength and climate calibration of a European tree-ring isotope network. *Geophys. Res. Lett.* **34** https://doi.org/10.1029/2007gl031106 (2007).
35. Treydte, K. et al. Climate signals in the European isotope network ISONET. *TRACE* **5**, 138–147 (2007).
36. Seftigen, K., Goosse, H., Klein, F. & Chen, D. Hydroclimate variability in Scandinavia over the last millennium – insights from a climate model–proxy data comparison. *Clim. Past* **13**, 1831–1850 (2017).
37. Trigo, R. M., Osborn, T. J. & Corte-Real, J. M. The North Atlantic Oscillation influence on Europe: climate impacts and associated physical mechanisms. *Clim. Res.* **20**, 9–17 (2002).
38. López-Moreno, J. I. & Vicente-Serrano, S. M. Positive and negative phases of the wintertime North Atlantic oscillation and drought occurrence over europe: a multitemporal-scale approach. *J. Clim.* **21**, 1220–1243 (2008).
39. López-Moreno, J. I. et al. *In:* Hydrological, socioeconomic and ecological impacts of the north atlantic oscillation in the mediterranean region advances in global change research. Chapter **6**, 73–89 (2011).
40. Tsanis, I. & Tapoglou, E. Winter North Atlantic Oscillation impact on European precipitation and drought under climate change. *Theor. Appl. Climatol.* **135**, 323–330 (2018).
41. Zhou, S. et al. Land-atmosphere feedbacks exacerbate concurrent soil drought and atmospheric aridity. *Proc. Natl. Acad. Sci. USA* **116**, 18848–18853 (2019).
42. Trouet, V., Babst, F. & Meko, M. Recent enhanced high-summer North Atlantic Jet variability emerges from three-century context. *Nat. Commun.* **9**, 180 (2018).
43. García-Herrera, R. et al. The European 2016/17 drought. *J. Clim.* **32**, 3169–3187 (2019).
44. Miralles, D. G., Teuling, A. J., van Heerwaarden, C. C. & Vilà-Guerau de Arellano, J. Mega-heatwave temperatures due to combined soil desiccation and atmospheric heat accumulation. *Nat. Geosci.* **7**, 345–349 (2014).
45. Schwingshackl, C., Hirschi, M. & Seneviratne, S. I. Quantifying spatiotemporal variations of soil moisture control on surface energy balance and near-surface air temperature. *J. Clim.* **30**, 7105–7124 (2017).
46. Seneviratne, S. et al. Investigating soil moisture–climate interactions in a changing climate: a review. *Earth-Sci. Rev.* **99**, 125–161 (2010).
47. Miralles, D. G., van den Berg, M. J., Teuling, A. J. & de Jeu, R. A. M. Soil moisture-temperature coupling: a multiscale observational analysis. *Geophys. Res. Lett.* **39**, L21707 (2012).
48. Poljanšek, S., Jevšenak, J., Gričar, J. & Levanič, T. Seasonal radial growth of black pine (Pinus nigra Arnold) from Bosnia and Herzegovina, monitored by the pinning method and manual band dendrometers. *Acta Silvae et Ligni* **119**, 1–11 (2019).
49. Poljanšek, S., Ballian, D., Nagel, T. A. & Levanič, T. A 435-year-long european black pine (Pinus nigra) chronology for the Central-Western Balkan Region. *Tree-Ring Res.* **68**, 31–44 (2012).
50. Holmes, R. L. Computer-assisted quality control in tree-ring dating and measurement. *Tree-Ring Bull.* **43**, 69–78 (1983).
51. Xu, C. et al. Asian-Australian summer monsoons linkage to ENSO strengthened by global warming. *npj Clim. Atmos. Sci.* **6**, 8 (2023).
52. Loader, N. J., Robertson, I., Barker, A. C., Switsur, V. R. & Waterhouse, J. S. An improved technique for the batch processing of small wholewood samples to α-cellulose. *Chem. Geol.* **136**, 313–317 (1997).
53. Green, J. W. *In*: Methods in carbohydrate chemistry. Vol. 3 (ed. R.W. Whiesler) 9–12 (Academic Press, 1963).
54. Fritts, H. Tree rings and climate. (Academic Press, 1976).
55. Cook, E. R., Meko, D. M., Stahle, D. W. & Cleaveland, M. K. Drought reconstructions for the continental United States. *J. Clim.* **12**, 1145–1162 (1999).
56. Durbin, J. & Watson, G. S. J. B. Testing for serial correlation in least squares regression: I. **37**, 409-428 (1950).
57. Kalnay, E. et al. The NCEP/NCAR 40-year reanalysis project. *Bull. Am. Meteorol. Soc.* **77**, 437–471 (1996).
58. Dai, A., Trenberth, K. E. & Qian, T. A global dataset of Palmer Drought Severity index for 1870–2002: relationship with soil moisture and effects of surface warming. *J. Hydrometeorol.* **5**, 1117–1130 (2004).
59. Harris, I., Osborn, T. J., Jones, P. & Lister, D. Version 4 of the CRU TS monthly high-resolution gridded multivariate climate dataset. *Sci. Data* **7**, 109 (2020).
60. Vicente-Serrano, S. M., Beguería, S., López-Moreno, J. I., Angulo, M. & El Kenawy, A. A new global 0.5° gridded dataset (1901–2006) of a multiscalar drought index: comparison with current drought index datasets based on the palmer drought severity index. *J. Hydrometeorol.* **11**, 1033–1043 (2010).
61. Raible, C. C., Barenbold, O. & Gomez-Navarro, J. J. Drought indices revisited – improving and testing of drought indices in a simulation of the last two millennia for Europe. *Tellus A: Dyn. Meteorol. Oceanogr.* **69** https://doi.org/10.1080/16000870.2017.1296226 (2017).
62. Yuan, S., Quiring, S. M. & Leasor, Z. T. Historical changes in surface soil moisture over the contiguous United States: an assessment of CMIP6. *Geophys. Res. Lett.* **48** https://doi.org/10.1029/2020gl089991 (2021).
63. Cook, E. R. et al. A Euro-Mediterranean tree-ring reconstruction of the winter NAO index since 910 C.E. *Clim. Dyn.* **53**, 1567–1580 (2019).
64. Muñoz-Sabater, J. et al. ERA5-Land: a state-of-the-art global reanalysis dataset for land applications. *Earth Syst. Sci. Data* **13**, 4349–4383 (2021).
65. Rodionov, S. N. A sequential algorithm for testing climate regime shifts. *Geophys. Res. Lett.* **31**, L09204 (2004).
66. Cohen, R. A. An introduction to PROC LOESS for local regression. (SUGI Proceedings, 1999).
67. Lorenz, R., Pitman, A., Hirsch, A. & Srbinovsky, J. Intraseasonal versus interannual measures of land–atmosphere coupling strength in a Global Climate Model: GLACE-1 versus GLACE-CMIP5 experiments in ACCESS1.3b. *J. Hydrometeorol.* **16**, 2276–2295 (2015).

68. Zhang, P. et al. Abrupt shift to hotter and drier climate over inner East Asia beyond the tipping point. *Science* **370**, 1095–1099 (2020).

Acknowledgements

This study was supported by the National Key Research and Development Program (2017YFE0112800), the National Natural Science Foundation of China (41888101, 41877457, 42022059), the Strategic Priority Research Program of the Chinese Academy of Sciences, China (Grant No. XDB26020000), the Key Research Program of the Institute of Geology and Geophysics (CAS Grant IGGCAS-201905), and the CAS Youth Interdisciplinary Team (JCTD-2021-05).

Author contributions

C.X. designed the study. Q.H., Z.G., and S.M. conceived the project. S.M., M.G., and Z.G. collected tree ring samples. W.A. conducted the cross-dating, cellulose extraction, and tree ring oxygen isotope measurement. W.A. performed most of the analyses with support from C.X., S.S., and Y.S. W.A. wrote the draft of the manuscript. All authors contributed to interpreting the results and discussions and revised the manuscript.

Competing interests

The authors declare no competing interests.

Additional information

Supplementary information The online version contains supplementary material available at https://doi.org/10.1038/s43247-023-00907-1.

Correspondence and requests for materials should be addressed to Chenxi Xu.

Peer review information *Communications Earth & Environment* thanks the anonymous reviewers for their contribution to the peer review of this work. Primary Handling Editors: Kyung-Sook Yun and Aliénor Lavergne.